Applied Surface Science 430 (2018) 639–646

Contents lists available at ScienceDirect

Applied Surface Science

journal homepage: www.elsevier.com/locate/apsusc

Full Length Article

One-step growth of nanosheet-assembled BiOCl/BiOBr microspheres for highly efficient visible photocatalytic performance

Jinfeng Zhang[a,1], Jiali Lv[a,1], Kai Dai[a,*], Changhao Liang[b,*], Qi Liu[c]

[a] College of Physics and Electronic Information, Anhui Key Laboratory of Energetic Materials, Huaibei Normal University, Huaibei, 235000, PR China
[b] Key Laboratory of Materials Physics and Anhui Key Laboratory of Nanomaterials and Nanotechnology, Institute of Solid State Physics, Hefei Institutes of Physical Science, Chinese Academy of Sciences, Hefei, 230031, PR China
[c] Key Laboratory of Microelectronic Devices & Integrated Technology, Institute of Microelectronics, Chinese Academy of Sciences, Beijing, 100029, PR China

ARTICLE INFO

Article history:
Received 5 January 2017
Received in revised form 10 February 2017
Accepted 13 February 2017
Available online 20 February 2017

Keywords:
Chemical preparation
Composites
Catalysis
Photocatalytic activity

ABSTRACT

In this work, we have developed a simple synthetic approach of nanosheet-assembled BiOCl/BiOBr microspheres by an ethylene glycol (EG)-assisted hydrothermal method. The crystalline form, morphology, chemical composition, optical performance and surface area of BiOCl/BiOBr microspheres were identified using X-ray diffraction (XRD), transmission electron microscopy (TEM), high resolution TEM (HRTEM), scanning electron microscopy (SEM), energy-dispersive X-ray spectroscopy spectra (EDX), UV–vis diffuse reflectance spectroscopy (DRS) analysis, high resolution X-ray photoelectron spectra (XPS) and N_2 adsorption-desorption isotherms. BiOCl/BiOBr microspheres were nanosheet-assembled particles, which possessed visible light absorption under LED light irridation. Additionally, the methylene blue (MB) photodegradation performance of different BiOCl/BiOBr microspheres irradiated under 410 nm LED light arrays were investigated, the results exhibited that as-prepared BiOCl/BiOBr products showed higher catalytic effiency than pure BiOCl or BiOBr. By optimizing the composition ration of the BiOCl and BiOBr, up to 93% degradation rate can be obtained in the 40%BiOCl/BiOBr microspheres. Finally, the photocatalytic mechanism of BiOCl/BiOBr microspheres had been proposed.

1. Introduction

Environmental organic pollution and energy needs are the major concern throughout the world at present. Semiconductor photocatalysis technique is a “green” method which completely eliminates the organic contamination in water and air because it provides innovative, low cost, catalyzed chemical oxidation processes for decomposing organic hazardous materials [1–7]. This transversion enables organic degradation and hydrogen and oxygen production via the generation of •OH radicals and other oxidative species [8–14]. Among photocatalytic materials, TiO_2 is always considered as the most promising photocatalysts because of excellent photocatalytic activity, high chemical and biological photostability, nontoxicity and relatively low-cost [15–18]. However, the photo-efficiency and the sunlight response range of TiO_2 are restricted because of the wide gap [19–24]. Until now, the design of efficient, simple, and long-life photocatalysts that work well under visible light (400 nm < λ < 760 nm) is a maximal challenge in this research work. More recently, various oxide, sulfide, multicomponent oxide or oxynitride based materials have been studied for photocatalystic utilization, such as Cu_2O [25,26], Ag_3PO_4 [27,28], Bi_2MoO_6 [6,29,30], AgBr [31,32], $AgGaO_2$ [33], C_3N_4 [6,34,35], WS_2 [36,37], $BiVO_4$ [38,39], $CaFe_2O_4$ [40], etc. They exhibit photocatalytic activity in the dyes or other organic pollution treatment under visible light excitation. However, the poor specific surface area of these materials prevents the industrial applications, and the rapid charge carrier recombination rate also seriously limits their photocatalytic efficiency.

Recently, bismuth oxyhalides (BiOX (X = I, Cl, Br)) have been extensively studied due to their special chemical and physical performance and potential value in sensors, catalysis, photology and so on [41–45]. All the BiOX compounds have tetragonal matlockite-type structure, this special layer structure is composed of $[Bi_2O_2^{2+}]$ slabs, which overlapped by halogen atoms [46–50].

Over the past few years, more attention has been paid to morphology-controlled synthesis of BiOX and to the preparation of BiOX-based composite used as photocatalyst materials in oxidation reaction fields, such as water splitting, dyes color removal, organic pollutants decomposition [51–54]. Chemical processes are

* Corresponding authors.
E-mail addresses: daikai940@chnu.edu.cn (K. Dai), chliang@issp.ac.cn (C. Liang).
[1] These authors contributed equally to this work.

http://dx.doi.org/10.1016/j.apsusc.2017.02.101
0169-4332/

the primary methods used for the fabrication of BiOBr or BiOCl nanomaterials, in which the solvothermal method is the most promising ways for fabricating the proper nanomaterial of ideal structure because of simple preparation, easy solution manipulation and energy saving. Nevertheless, facile design of high-quality BiOX nanocomposites with satisfactory photocatalytic performanc via an easy synthetic process is still a great challenging problem.

In the present study, we fabricated nanosheet-assembled BiOCl/BiOBr microspheres via a facile one-step thermal technology at 120 °C and characterized the BiOCl/BiOBr heterojunction structures. The photocatalytic property of BiOCl/BiOBr microsphere was investigated by methylene blue (MB) photodegradation under irradiation of 410 nm light-emitting diode (LED) arrays light. Moreover, the catalytic mechanism of BiOCl/BiOBr microsphere was put forward based on the special heterojunction structure.

2. Material and methods

2.1. Preparation

0.8 mmol $Bi(NO_3)_3{\cdot}5H_2O$, 0.8 mmol KX(X = Br, Cl), 2 mL water and 38 mL EG were magnetic stirred to form the mixture, and subsequently transferred into 50 mL Teflon-lined autoclave. After that, the mixture was heated at 120 °C for 6 h in air dry oven. BiOCl/BiOBr samples with different molar weight in Cl/Bi ratios (from 0% to 100%) were separated by centrifugation, and finally dried in electric vacuum drying oven.

2.2. Characterization

The structure of synthesized architecture BiOCl/BiOBr was observed using JEOL-2010 high-resolution transmission electron microscopy (HRTEM). Total organic carbon (TOC) analyzer was recorded by Elementar Liqui TOC II. X-ray diffraction (XRD) data for BiOX samples were collected by a PANalytical Empyrean/X'pert MRD at room temperature. Scanning electron microscopy (SEM) of as-prepared BiOCl/BiOBr was investigated by using X-650. The X-ray photoelectron spectra (XPS) of BiOCl/BiOBr composite were collected by Thermo ESCALAB-250. The BET specific surface area values of BiOX were tested by Micromeritics ASAP-2010 system. The optical properties of BiOCl/BiOBr composites were analyzed by FLS-920 photoluminescence (PL) spectra and PerkinElmer Lambda-950 UV–vis-IR spectrophotometer.

2.3. Photocatalytic progress

The experimental progress was tested in 50 mL quartz glass including 30 mL MB solution (10 mg/L) and 0.03 g BiOX samples. Before visible LED light irradiation, quartz glass was magnetically stirred in the dark under room temperature in order to build the adsorption-desorption equilibrium. Then, BiOCl/BiOBr samples were excited by LED light arrays. The photodegradation efficiency and photocatalytic procedure of MB solution were calculated as follows:

$$\eta = \frac{C_0 - C}{C_0} \times 100\% \quad (1)$$

$$\ln \frac{C_0}{C} = k_{app} t \quad (2)$$

Where: C_0 is the absorbance value of initial MB dye solution, C is the absorbance value of the MB solution after 410 nm LED light irradiation and k_{app} is the apparent pseudo-first-order rate constant.

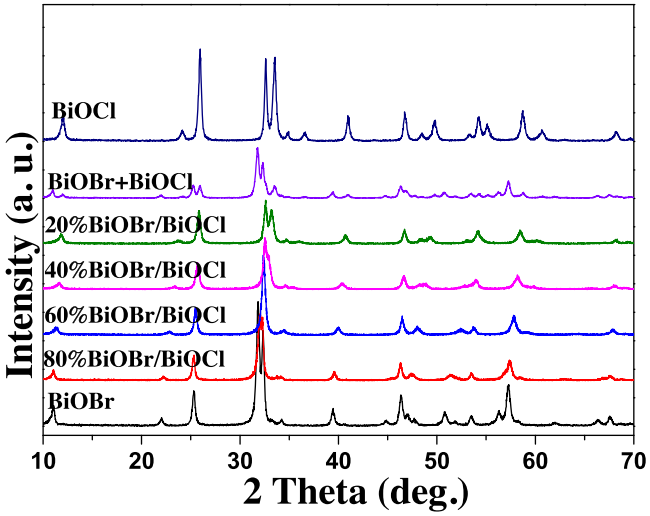

Fig. 1. XRD patterns of different photocatalysts.

3. Results and discussion

XRD is an accurate, rapid and nondestructive technique used for crystalline phase analysis of photocatalysts. Fig. 1 shows the XRD patterns of BiOCl/BiOBr with different ratios of Cl/Br. As comparison, physical mixed BiOCl and BiOBr (weight ratio is 40:60) labeled as BiOCl+BiOBr is also tested. All the peaks of BiOCl, BiOBr and BiOCl/BiOBr composites were distinguishable. The characteristic peaks of BiOBr at 10.8°, 21.8°, 25.2°, 31.6°, 32.1°, 34.0°, 39.3°, 46.2°, 50.6°, 53.4°, 56.2°, 57.1°, 66.2° and 67.4° were observed and can be respectively indexed to the (0 0 1), (0 0 2), (1 0 1), (1 0 2), (1 1 0), (1 1 1), (1 1 2), (2 0 0), (1 0 4), (2 1 1), (1 1 4), (2 1 2), (2 0 4) and (2 2 0) of tetragonal BiOBr (JCPDS No. 78-0348), and the diffraction peaks of BiOCl at 11.8°, 24.1°, 25.8°, 32.5°, 33.3°, 34.6°, 36.5°, 40.8°, 46.6°, 48.3°, 49.6°, 54.0°, 55.1°, 53.1°, 58.5°, 60.4° and 68.0° can be indexed to the (0 0 1), (0 0 2), (1 0 1), (1 1 0), (1 0 2), (1 1 1), (0 0 3), (1 1 2), (2 0 0), (2 0 1), (1 1 3), (2 1 1), (1 0 4), (2 0 2), (2 1 2), (1 1 4) and (2 2 0) with tetragonal BiOCl (JCPDS No. 06-0429). For the BiOCl/BiOBr composites, the intensity of BiOBr peaks increased gradually with the increase contents of BiOBr in BiOCl/BiOBr, at the same time, the peaks of BiOCl weakened simultaneously for its abatement. No other impurity peaks were found, indicating that BiOCl/BiOBr nanocomposites are only made up of BiOCl and BiOBr phases.

Fig. 2a, b and c display the SEM images of BiOCl, 40%BiOCl/BiOBr and BiOBr microsphere samples, respectively. These microspheres are loosely assembled by nanosheets. Fig. 2d, 2e and 2f show the EDX spectrum of as-synthesized BiOCl, BiOBr and BiOCl/BiOBr, respectively. The EDX pattern shows that all of the as-synthesized photocatalysts are very pure. 40%BiOCl/BiOBr microsphere is further revealed by TEM images in Fig. 2g, from which it is apparent that the structure is assembled by some nanosheets. Fig. 2h shows the HRTEM image of 40%BiOCl/BiOBr microsphere, it can be found that two sets of lattices are present with interfringe spacings of 0.276 nm and 0.285 nm, corresponding to BiOBr (0 0 1) and BiOCl (1 1 0) planes, respectively.

The XPS spectra for C1s, Bi4f, O1s, Cl2p and Br3d of 40%BiOCl/BiOBr have shown in Fig. 3a. The C peak is from the organic pollution of XPS instrument. As indicated in Fig. 3b, two peaks centered at 159.90 and 165.12 eV are Bi4f7/2 and Bi4f5/2, which confirms Bi^{3+} ions in BiOCl/BiOBr composites [55]. Fig. 3c shows the binding energy of 530.31 eV, which was assigned to O1s. As indicated in Fig. 3d, the Cl2p peak is associated with binding energy of 197.91 eV, which is characteristic of Cl^- in BiOCl [56].

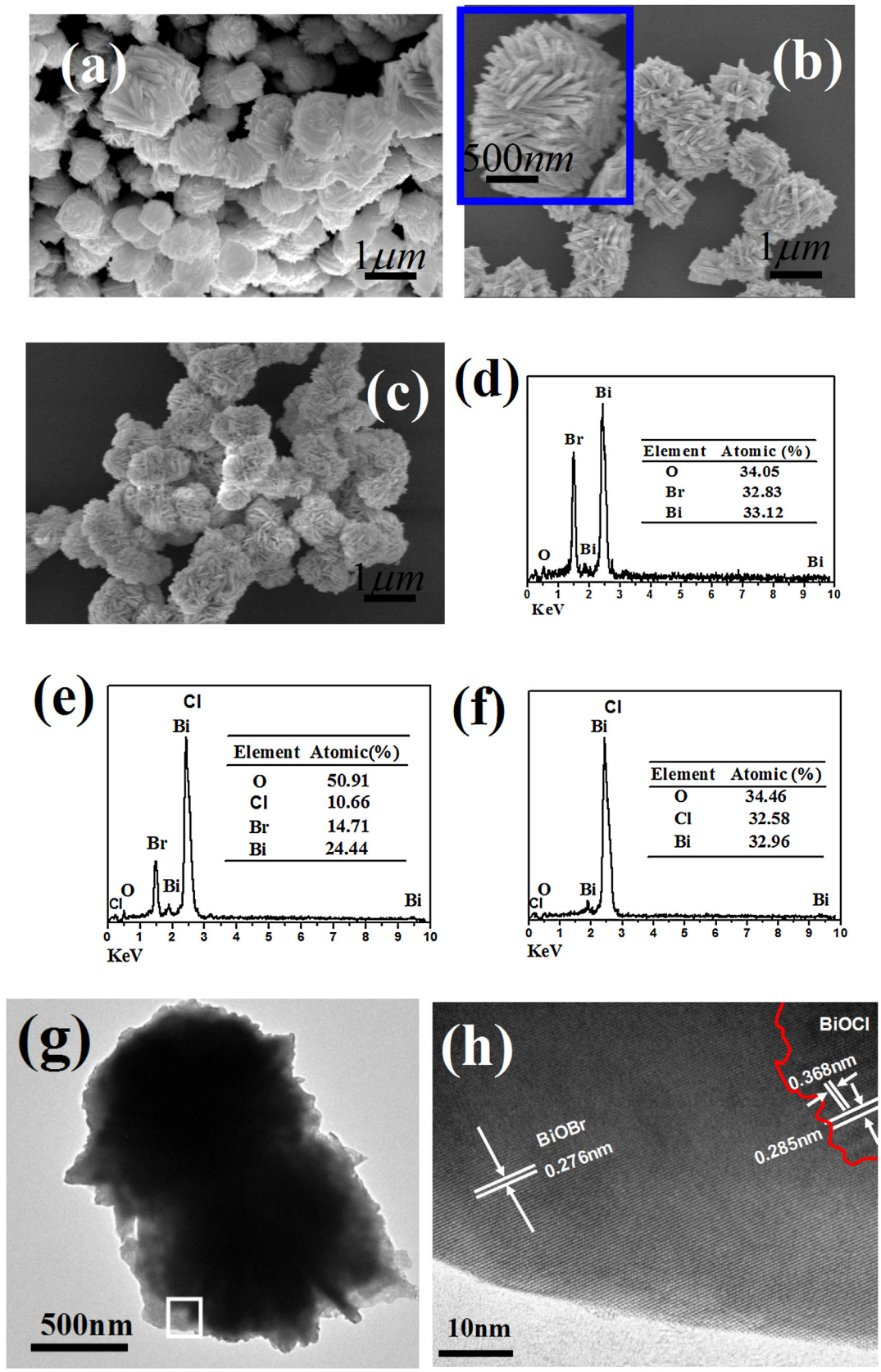

Fig. 2. SEM images of (a) BiOCl, (b) 40%BiOCl/BiOBr and (c) BiOBr, EDX spectra of (d) BiOCl, (e) 40%BiOCl/BiOBr and (f) BiOBr, and TEM (g) and HRTEM (h) images of 40%BiOCl/BiOBr.

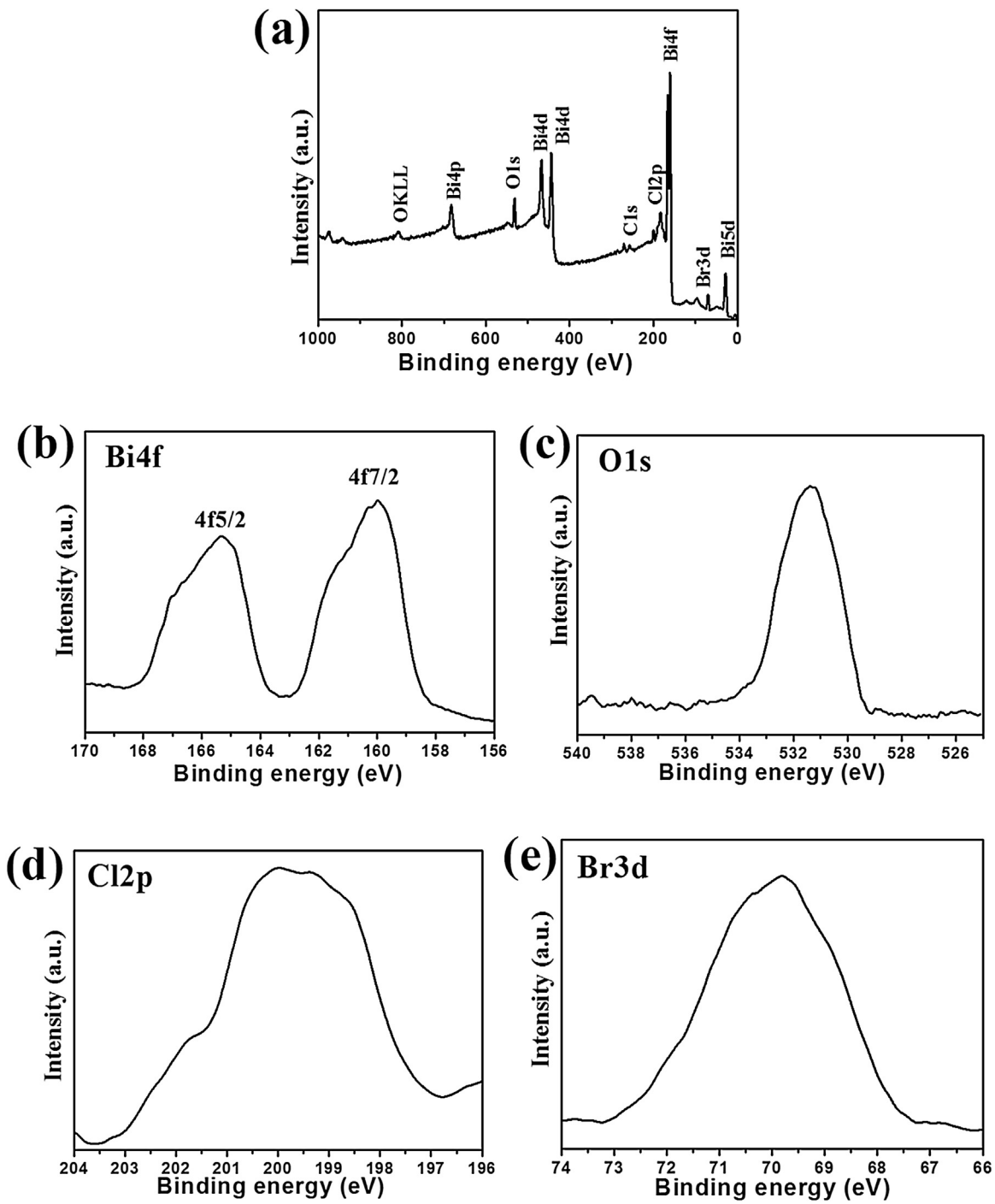

Fig. 3. XPS spectra of the as-prepared 40%BiOCl/BiOBr composite (a) survey spectrum, (b) Bi4f, (c) O1s, (d) Cl2p and (e) Br3d.

On the other hand, as indicated in Fig. 3e, the XPS signal of Br3d at binding energy 68.17 eV is characteristic for Br^- anions [57]. Therefore, both XRD and XPS results are evidences that the coexistence of BiOCl and BiOBr is achieved in the BiOCl/BiOBr microspheres.

UV–vis diffuse reflectance spectroscopy (DRS) of the different photocatalysts has been shown in Fig. 4a. According to the absorption spectra, E_g of semiconductors can be calculated from the following equation [58,59]:

$$\alpha(h\nu) = A\left(h\nu\text{-}\mathrm{E}_g\right)^2 \quad (3)$$

Where: α and ν are the absorption coefficient and light frequency of the semiconductor, respectively. According to Fig. 4b and Eq. (3), E_g of BiOCl and BiOBr are 3.31 and 2.73 eV, respectively.

According to the above discussion, the formation progress of BiOX microsphere could be proposed by the three stages in Fig. 5. As indicated in Fig. 5a, at first stage, Bi^{3+} ions will react with Cl^- or/and Br^- and forming BiOX nuclei, water will supply O element. In the sequence stage, as indicated in Fig. 5b, quasi two-dimensional BiOX nanosheets could be formed to reduce the surface energy [60]. At last, as indicated in Fig. 5c, under the action of EG, the excess BiOX nanosheets will grow in miniemulsion interface and then self-assembly to form the BiOCl/BiOBr hybrid composites.

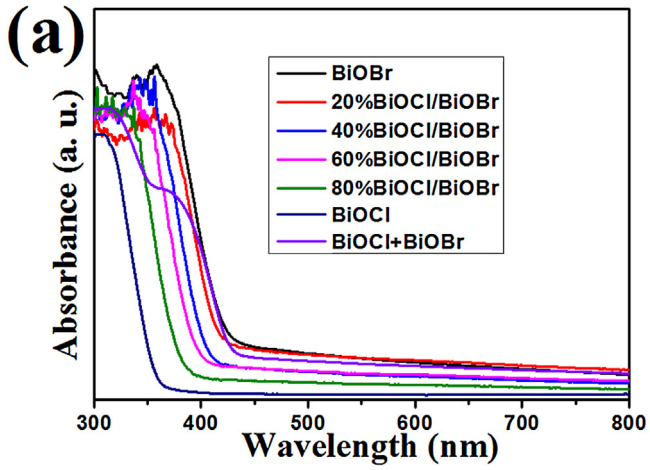

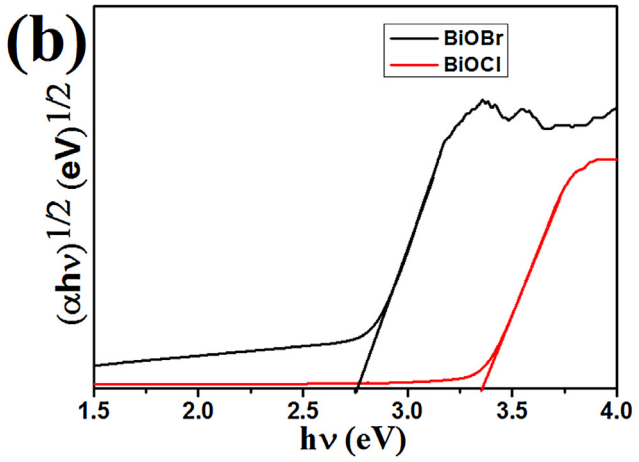

Fig. 4. (a) UV–vis DRS of the as-prepared samples and (b) the band gaps (E_g) of BiOBr and BiOCl.

Table 1
Data of S_{BET} and PSV of samples.

Sample	S_{BET} (m^2/g)	PSV (cm^3/g)
BiOCl	18.4	0.020
40%BiOCl/BiOBr	17.8	0.017
BiOBr	17.2	0.015

Fig. 6 shows N_2 adsorption-desorption isotherms for BiOCl, 40%BiOCl/BiOBr and BiOBr at 77 K. Table 1 shows the data of BET surface area (S_{BET}) and pore specific volume (PSV), we can found that S_{BET} and PSV of catalysts did not show obvious difference.

The photocatalytic performance of BiOX microsphere was investigated by photodegradation of MB solution. As indicated in Fig. 7a,

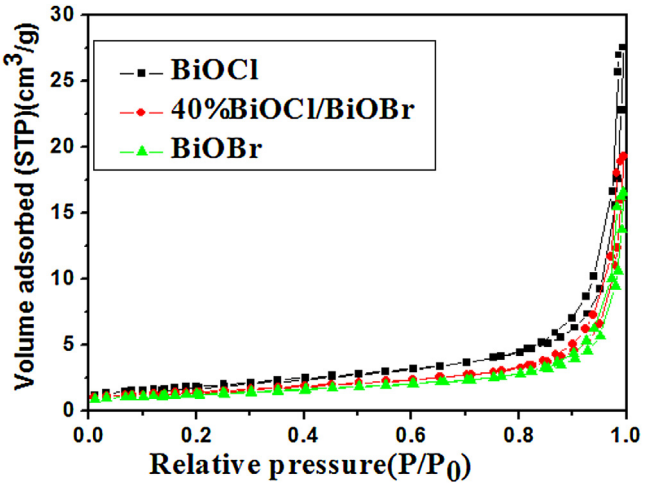

Fig. 6. Isotherms for Nitrogen adsorption-desorption.

the corresponding adsorption properties for dye in the dark on P25, BiOCl, 20%BiOCl/BiOBr, 40%BiOCl/BiOBr, 60%BiOCl/BiOBr, 80%BiOCl/BiOBr and BiOBr were respectively 8%, 3.8%, 3.3%, 3.0%, 2.8%, 2.7% and 2.4%. When 40%BiOCl/BiOBr was excited by 410 nm LED light, 93% of MB dye was photodegradated in 6 h. At the same time, the degradation of MB on P25, BiOCl, 20%BiOCl/BiOBr, 60%BiOCl/BiOBr, 80%BiOCl/BiOBr and BiOBr suspension were only 17%, 10%, 83%, 77%, 45%, and 72%, respectively. Fig. 7b shows spectra evolution of MB over 40%BiOCl/BiOBr 6 h. Linear transform $ln(C_0/C)$ curves of MB degradation was shown in Fig. 7c. According to equation (2), as indicated in Fig. 7d, k_{app} of MB degradation are 0.016, 0.2, 0.26, 0.41, 0.22, 0.09 and 0.01 h^{-1} for P25, BiOBr, 20%BiOCl/BiOBr, 40%BiOCl/BiOBr, 60%BiOCl/BiOBr, 80%BiOCl/BiOBr and BiOCl, respectively. 40%BiOCl/BiOBr showed the higher photocatalytic performance than other catalysts. To investigate MB mineralization completely, Fig. 7e shows TOC curves of MB solution, 40%BiOCl/BiOBr exhibited higher photocatalytic activity than other BiOCl/BiOBr composites and P25 TiO_2.

PL spectra are always used to demonstrate the migration and separation processes of photogenerated carriers. As indicated in Fig. 8, the main emission peaks are centered at ca. 388 and 426 nm for BiOCl and BiOBr, respectively. The emission intensity of BiOBr sample is lower than that of BiOCl. For BiOCl/BiOBr composites, 40%BiOCl/BiOBr has the lowest emission intensity. Thus, 40%BiOCl/BiOBr has the lowest recombination rate. This result is according with the photocatalytic test.

As indicated in Fig. 7a, the MB absorption abilities of the BiOX microsphere did not show obvious difference, which indicates that the key influential factor for the improved degrading efficiency is the special composite structure rather than BET surface area or absorbance capacity. When the content of BiOCl in BiOCl/BiOBr increased from 20% to 40%, more interface of BiOCl-BiOBr

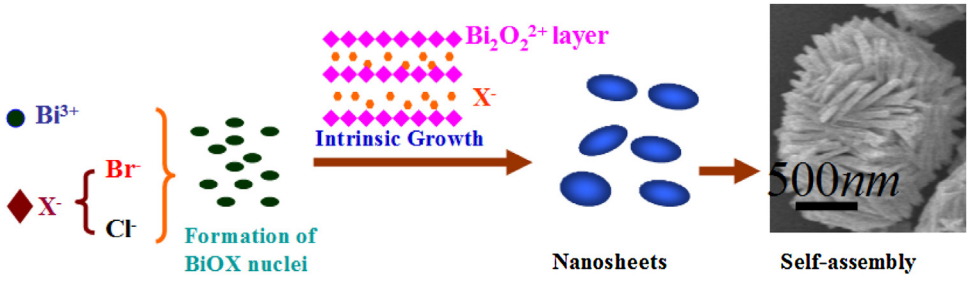

Fig. 5. Schematic illustration of the possible formation process of BiOX microphere.

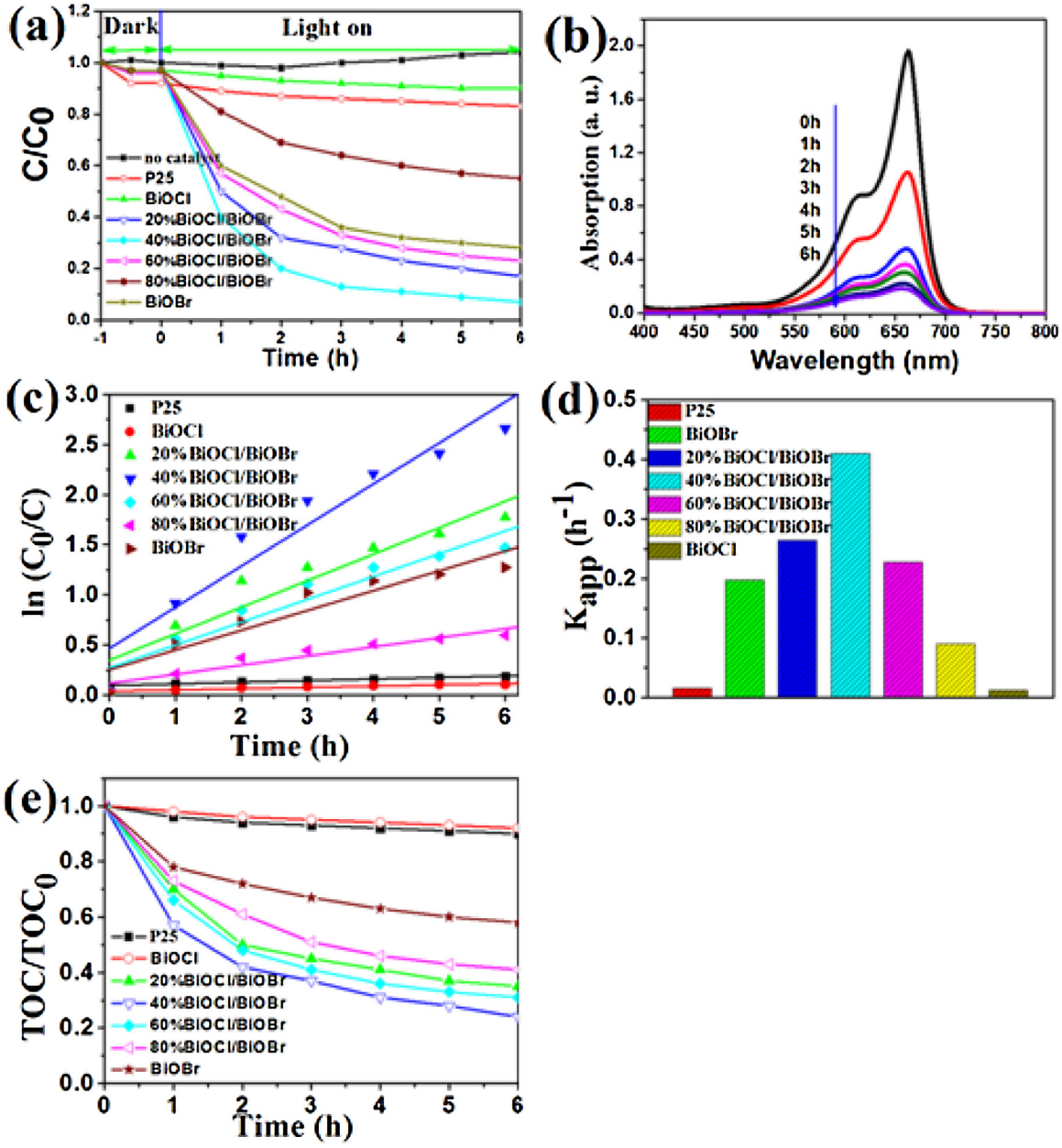

Fig. 7. (a) Photocatalytic degradation of MB under 410 nm LED light irradiation, (b) Temporal evolution of MB absorption spectrum over 40%BiOCl/BiOBr, (c) linear transform $\ln(C_0/C)$ of the kinetic curves of MB degradation, (d) the apparent pseudo-first-order rate constant k_{app} with different catalysts and (e) TOC removal by different catalysts.

heterojunction will be appeared, which will promote photoinduced electron (e^-) and hole (h^+) pairs separation and thus increase the photodegradation efficiency. If the content of BiOCl added continuously, the BiOCl-BiOBr interface will decrease and the excessive BiOCl with narrow band-gap will be served as the recombination center of e^--h^+ pairs, which will lower catalytic performance. Thus, 40%BiOCl/BiOBr with an optimal proportion of BiOCl to BiOBr exhibited the highest photocatalytic performance.

It is generally believed that photocatalytic processes are based on e^- and h^+ pairs efficient generation and separation [61]. The valence band potentials (VB) of semiconductor materials can be theoretically calculated as the following formula [62]:

$$E_{VB} = X - E^c + 0.5E_g \quad (4)$$

Where: E_{VB}, X and E^c are VB edge potential, electronegativity of the semiconductor materials and the energy of free electrons on the hydrogen scale (about 4.5 eV), respectively. Moreover, the conduction band (CB) edge potential (E_{CB}) can be obtained by $E_{CB} = E_{VB} - E_g$. The X values for the BiOCl and BiOBr materials are 6.360 and 6.176 eV, respectively. According to Eq. (4), E_{VB} values of BiOCl and BiOBr are 3.52 and 3.04 eV, respectively. Thus, the E_{CB} of BiOCl and BiOBr are 0.21 and 0.31 eV, respectively.

Based on the above studies, Fig. 9 shows the energy band structure of BiOCl/BiOBr microspheres and photocatalytic reaction process under 410 nm LED light irradiation. For BiOBr itself, BiOBr can be irridated under 410 nm LED light (ca. 3.02 eV) and induce to generate e^- and h^+ pairs. However, e^- and h^+ recombined rapidly due to the narrow band-gap and large size. But BiOCl will not be activated under 410 nm LED light irradiation. As indicated in Fig. 9, when BiOCl/BiOBr composite was irridated by the 410 nm visible LED light, BiOBr could be excited, the e^- in the VB of BiOBr semconductor could be subsequently irridated up to a higher potential edge (ca. 0.1 eV) [63]. The e^- on the outer surface of BiOBr will easily transfer to CB of BiOCl because CB value of BiOBr (0.1 eV) is more

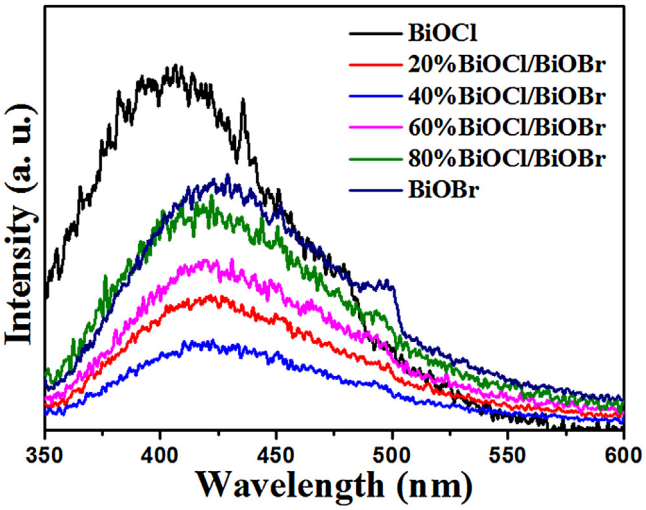

Fig. 8. The PL spectra of different BiOCl/BiOBr microspheres.

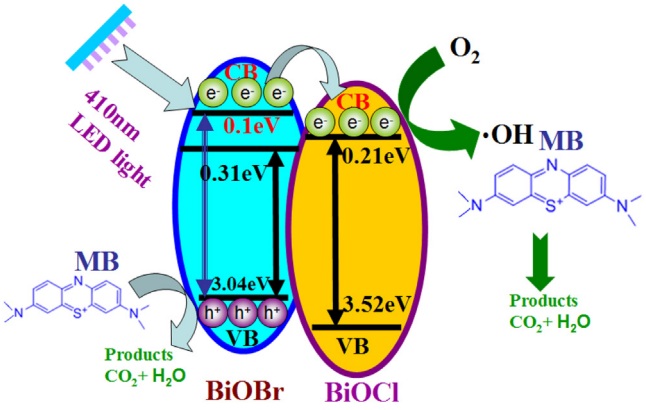

Fig. 9. Schematic illustration of the BiOBr/BiOCl photocatalytic reaction process under 410 nm LED light irradiation.

negative than that of BiOCl (0.21 eV), leaving h^+ on VB of BiOBr. By this way, e^--h^+ pairs can be easily separated. Furthermore, the formed heterojunction between BiOBr and BiOCl in the BiOCl/BiOBr microspheres can hinder the fast recombination velocities between e^- and h^+, thus more effective e^- and h^+ pairs will take part in the photocatalytic process. Accordingly, the BiOCl/BiOBr composites show higher photocatalytic efficiency than that of single BiOCl and BiOBr. However, with the content of BiOCl in BiOCl/BiOBr being in excess, numerous photoinduced e^--h^+ pairs would recombine easily on the surface of BiOBr. Therefore, 40%BiOCl/BiOBr microspheres exhibited the best photocatalytic performance among the other photocatalysts.

4. Conclusions

In summary, nanosheet-assembled BiOCl/BiOBr microspheres were fabricated by facile solvothermal approach under low temperature. BiOCl/BiOBr composite exhibited enhanced photodegrading efficiency compared to single BiOBr and BiOCl over the photodegradation of MB dye. The efficient separation of e^- and h^+ originated from the formation of BiOCl/BiOBr heterojunction interface benefited to obtain higher photocatalytic activity. It is believed that nanosheet-assembled BiOCl/BiOBr microsphere is a kind of visible-light-driven photocatalysis for elimination of organic contaminants in our environment.

Acknowledgments

This work was supported by the National Natural Science Foundation of China (51572103 and 51502106), the Foundation for Young Talents in College of Anhui Province (12600941), Leading talent of Anhui Province, Innovation Team of Design and Application of Advanced Energetic Materials and Collaborative Innovation Center of Advanced Functional Materials (XTZX103732015008).

References

[1] W.L. Yu, J.F. Zhang, T.Y. Peng, New insight into the enhanced photocatalytic activity of N-, C- and S-doped ZnO photocatalysts, Appl. Catal. B: Environ. 181 (2016) 220–227.
[2] W.J. Ong, L.L. Tan, S.P. Cha, S.T. Yong, A.R. Mohamed, Facet-Dependent Photocatalytic Properties of TiO_2-Based Composites for Energy Conversion and Environmental Remediation, ChemSusChem 7 (2014) 690–719.
[3] M.A. Fox, M.T. Dulay, Heterogeneous photocatalysis, Chem. Rev. 93 (1993) 341–357.
[4] J.F. Zhang, S. Wageh, A. Al-Ghamdic, J.G. Yu, New understanding on the different photocatalytic activity of wurtzite and zinc-blende CdS, Appl. Catal. B: Environ. 192 (2016) 101–107.
[5] P. Zhou, J. Yu, M. Jaroniec, All-solid-state Z-scheme photocatalytic systems, Adv. Mater. 26 (2014) 4920–4935.
[6] J. Lv, K. Dai, J. Zhang, L. Geng, C. Liang, Q. Liu, G. Zhu, C. Chen, Facile synthesis of Z-scheme graphitic-C_3N_4/Bi_2MoO_6 nanocomposite for enhanced visible photocatalytic properties, Appl. Surf. Sci. 358 (2015) 377–384.
[7] R.A. He, S.W. Cao, J.G. Yu, Recent advances in morphology control and surface modification of Bi-based photocatalysts, Acta Phys. Chim. Sin. 32 (2016) 2841–2870.
[8] A. Fujishima, K. Honda, Electrochemical photolysis of water at a semiconductor electrode, Nature 238 (1972) 37–38.
[9] Q.J. Xiang, B. Cheng, J.G. Yu, Graphene-based photocatalysts for solar-fuel generation, Angew. Chem. Int. Ed. 54 (2015) 2–19.
[10] Q. Li, X. Li, S. Wageh, A.A. Al-Ghamdi, J. Yu, CdS/Graphene nanocomposite photocatalysts, Adv. Energy Mater. 5 (2015) 1500010.
[11] M.R. Hoffmann, S.T. Martin, W. Choi, D.W. Bahnemannt, Environmental applications of semiconductor photocatalysis, Chem. Rev. 95 (1995) 69–96.
[12] A. Kudo, Y. Miseki, Heterogeneous photocatalyst materials for water splitting, Chem. Soc. Rev. 38 (2009) 253–278.
[13] X. Li, J.G. Yu, J.X. Low, Y.P. Fang, J. Xiao, X.B. Chen, Engineering heterogeneous semiconductors for solar water splitting, J. Mater. Chem. A 3 (2015) 2485–2534.
[14] K. Zhang, L.J. Guo, Metal sulphide semiconductors for photocatalytic hydrogen production, Catal. Sci. Technol. 3 (2013) 1672–1690.
[15] A. Fujishima, T.N. Rao, D.A. Tryk, Titanium dioxide photocatalysis, J. Photochem. Photobiol. C 1 (2000) 1–21.
[16] J.F. Zhang, P. Zhou, J.J. Liu, J.G. Yu, New understanding of the difference of photocatalytic activity among anatase, rutile and brookite TiO_2, Phys. Chem. Chem. Phys. 16 (2014) 20382–20386.
[17] Q.L. Xu, J.G. Yu, J. Zhang, J.f. Zhang, G. Liu, Cubic anatase TiO_2 nanocrystals with enhanced photocatalytic CO_2 reduction activity, Chem. Commun. 51 (2015) 7950–7953.
[18] K. Lv, S. Fang, L. Si, Y. Xia, W. Ho, M. Li, Fabrication of TiO_2 nanorod assembly grafted rGO (rGO@TiO_2-NR) hybridized flake-like photocatalyst, Appl. Surf. Sci. 391 (2017) 218–227.
[19] J.S. Zhong, J.R. Xu, Q.Y. Wang, Nitrogen and vanadium Co-doped TiO_2 mesosponge layers for enhancement in visible photocatalytic activity, Appl. Surf. Sci. 315 (2014) 131–137.
[20] J.G. Yu, J.X. Low, W. Xiao, P. Zhou, M. Jaroniec, Enhanced photocatalytic CO_2-reduction activity of anatase TiO_2 by coexposed {001} and {101} facets, J. Am. Chem. Soc. 136 (2014) 8839–8842.
[21] W.J. Ong, L.L. Tan, S.P. Chai, S.T. Yong, A.R. Mohamed, Highly reactive {001} facets of TiO_2-based composites: synthesis, formation mechanism and characterization, Nanoscale 6 (2014) 1946–2008.
[22] D.O. Scanlon, C.W. Dunnill, J. Buckeridge, S.A. Shevlin, A.J. Logsdail, S.M. Woodley, C.R.A. Catlow, M.J. Powell, R.G. Palgrave, I.P. Parkin, Graeme W. Watson, T. Keal, P. Sherwood, A. Walsh, A.A. Sokol, Band alignment of rutile and anatase TiO_2, Nat. Mater. 12 (2013) 798–801.
[23] K. Dai, L. Lu, C. Liang, Q. Liu, G. Zhu, Heterojunction of facet coupled g-C3N4/surface-fluorinated TiO_2 nanosheets for organic pollutants degradation under visible LED light irradiation, Appl. Catal. B: Environ. 156–157 (2014) 331–340.
[24] Z.a. Huang, Q. Sun, K. Lv, Z. Zhang, M. Li, B. Li, Effect of contact interface between TiO_2 and g-C_3N_4 on the photoreactivity of g-C_3N_4/TiO_2 photocatalyst: (001) vs (101) facets of TiO_2, Appl. Catal. B: Environ. 164 (2015) 420–427.
[25] L. Xu, H. Xu, S.B. Wu, X.Y. Zhang, Synergy effect over electrodeposited submicron Cu_2O films in photocatalytic degradation of methylene blue, Appl. Surf. Sci. 258 (2012) 4934–4938.
[26] J. Yu, H. Yu, S. Liu, S. Mann, Template-free hydrothermal synthesis of CuO/Cu_2O composite hollow microspheres, Chem. Mater. 19 (2007) 4327–4334.

[27] N. Umezawa, O. Shuxin, J.H. Ye, Theoretical study of high photocatalytic performance of Ag_3PO_4, Phys. Rev. B 83 (2011) 035202.
[28] J. Zhang, J. Lv, K. Dai, Q. Liu, C. Liang, G. Zhu, Facile and green synthesis of novel porous g-C_3N_4/Ag_3PO_4 composite with enhanced visible light photocatalysis, Ceram. Int. 43 (2017) 1522–1529.
[29] Z. Wang, J. Iv, K. Dai, L. Lu, C. Liang, L. Geng, Large scale and facile synthesis of novel Z-scheme Bi_2MoO_6/Ag_3PO_4 composite for enhanced visible light photocatalyst, Mater. Lett. 169 (2016) 250–253.
[30] S.Y. Wang, X.L. Yang, X.H. Zhang, X. Ding, Z.X. Yang, K. Dai, H. Chen, A plate-on-plate sandwiched Z-scheme heterojunction photocatalyst: biOBr-Bi_2MoO_6 with enhanced photocatalytic performance, Appl. Surf. Sci. 391 (2017) 194–201.
[31] J.F. Zhang, T. Zhang, Preparation and characterization of highly efficient and stable visible-light-responsive photocatalyst AgBr/Ag_3PO_4, J. Nanomater. 2013 (2013) 565074.
[32] K. Dai, L. Lu, J. Dong, Z. Ji, G. Zhu, Q. Liu, Z. Liu, Y. Zhang, D. Li, C. Liang, Facile synthesis of a surface plasmon resonance-enhanced Ag/AgBr heterostructure and its photocatalytic performance with 450 nm LED illumination, Dalton Trans. 42 (2013) 4657–4662.
[33] Y. Maruyama, H. Irie, K. Hashimoto, Visible light sensitive photocatalyst, delafossite structured r-$AgGaO_2$, J. Phys. Chem. B 110 (2006) 23274–23278.
[34] S. Ye, R. Wang, M.Z. Wu, Y.P. Yuan, A review on g-C_3N_4 for photocatalytic water splitting and CO_2 reduction, Appl. Surf. Sci. 358 (2015) 15–27.
[35] S.W. Cao, J.X. Low, J.G. Yu, M. Jaroniec, Polymeric photocatalysts based on graphitic carbon nitride, Adv. Mater. 27 (2015) 2150–2176.
[36] J.C.Y. Wingkei Ho, Jun Lin, Jiaguo Yu, Puishan Li, Preparation and photocatalytic behavior of MoS_2 and WS_2 nanocluster sensitized TiO_2, Langmuir 20 (2004) 5865–5869.
[37] Y. Zhong, G. Zhao, F. Ma, Y. Wu, X. Hao, Utilizing photocorrosion-recrystallization to prepare a highly stable and efficient CdS/WS_2 nanocomposite photocatalyst for hydrogen evolution, Appl. Catal. B: Environ. 199 (2016) 466–472.
[38] P. Madhusudan, J.R. Ran, J. Zhang, J.G. Yu, G. Liu, Novel urea assisted hydrothermal synthesis of hierarchical $BiVO_4$/$Bi_2O_2CO_3$ nanocomposites with enhanced visible-light photocatalytic activity, Appl. Catal. B: Environ. 110 (2011) 286–295.
[39] Z.Y. Zhao, Z.S. Li, Z.G. Zou, Structure and energetics of low-index stoichiometric monoclinic clinobisvanite $BiVO_4$ surfaces, RSC Adv. 1 (2011) 874–883.
[40] S. Vadivel, D. Maruthamani, A. Habibi-Yangjeh, B. Paul, S.S. Dhar, K. Selvam, Facile synthesis of novel $CaFe_2O_4$/g-C_3N_4 nanocomposites for degradation of methylene blue under visible-light irradiation, J. Colloid Interface Sci. 480 (2016) 126–136.
[41] R. He, S. Cao, D. Guo, B. Cheng, S. Wageh, A.A. Al-Ghamdi, J. Yu, 3D BiOI–GO composite with enhanced photocatalytic performance for phenol degradation under visible-light, Ceram. Int. 41 (2015) 3511–3517.
[42] Z.Y. Zhao, W.W. Dai, Structural, electronic, and optical properties of Eu-doped BiOX (X = F, Cl, Br, I): a DFT+U study, Inorg. Chem. 53 (2014) 13001–13011.
[43] L.J. Zhao, X.C. Zhang, C.M. Fan, Z.H. Liang, P.D. Han, First-principles study on the structural, electronic and optical properties of BiOX (X = Cl Br, I) crystals, Phys. B 407 (2012) 3364–3370.
[44] W.I. Huang, Electronic structures and optical properties of BiOX (X = F, Cl, Br, I) via DFT calculations, J. Comput. Chem. 30 (2009) 1882–1891.
[45] Y.F. Zhang, M. Park, H.Y. Kim, B. Ding, S.J. Park, In-situ synthesis of nanofibers with various ratios of $BiOCl_x$/$BiOBr_y$/BiOlz for effective trichloroethylene photocatalytic degradation, Appl. Surf. Sci. 384 (2016) 192–199.
[46] M. Pan, H. Zhang, G. Gao, L. Liu, W. Chen, Facet-dependent catalytic activity of nanosheet-assembled bismuth oxyiodide microspheres in degradation of bisphenol A, Environ. Sci. Technol. 49 (2015) 6240–6248.
[47] A. Dash, S. Sarkar, V.N.K.B. Adusumalli, V. Mahalingam, Microwave synthesis, photoluminescence, and photocatalytic activity of PVA-functionalized Eu^{3+}-doped BiOX (X = Cl Br, I) nanoflakes, Langmuir 30 (2014) 1401–1409.
[48] H. Li, J. Shang, Z. Ai, L. Zhang, Efficient visible light nitrogen fixation with BiOBr nanosheets of oxygen vacancies on the exposed {001} facets, J. Am. Chem. Soc. 137 (2015) 6393–6399.
[49] X.N. Wang, W.L. Bi, P.P. Zhai, X.B. Wang, H.J. Li, G. Mailhot, W.B. Dong, Adsorption and photocatalytic degradation of pharmaceuticals by $BiOCl_xI_y$ nanospheres in aqueous solution, Appl. Surf. Sci. 360 (2016) 240–251.
[50] Q. Qin, Y.N. Guo, D.D. Zhou, Y.X. Yang, Y.H. Guo, Facile growth and composition-dependent photocatalytic activity of flowerlike $BiOCl_{1-x}Br_x$ hierarchical microspheres, Appl. Surf. Sci. 390 (2016) 765–777.
[51] M. Li, H. Huang, S. Yu, N. Tian, F. Dong, X. Du, Y. Zhang, Simultaneously promoting charge separation and photoabsorption of BiOX (X = Cl, Br) for efficient visible-light photocatalysis and photosensitization by compositing low-cost biochar, Appl. Surf. Sci. 386 (2016) 285–295.
[52] L. Ji, H. Wang, R. Yu, Heterogeneous photocatalysts BiOX/$NaBiO_3$ (X = Cl, Br, I): Photo-generated charge carriers transfer property and enhanced photocatalytic activity, Chem. Phys. 478 (2016) 14–22.
[53] Y. Bai, T. Chen, P. Wang, L. Wang, L. Ye, X. Shi, W. Bai, Size-dependent role of gold in g-C_3N_4/BiOBr/Au system for photocatalytic CO_2 reduction and dye degradation, Sol. Energy Mater. Sol. Cells 157 (2016) 406–414.
[54] K. Dai, L. Lu, C. Liang, G. Zhu, Q. Liu, L. Geng, J. He, A high efficient graphitic-C_3N_4/BiOI/graphene oxide ternary nanocomposite heterostructured photocatalyst with graphene oxide as electron transport buffer material, Dalton Trans. 44 (2015) 7903–7910.
[55] J. Zhang, J. Xia, S. Yin, H. Li, H. Xu, M. He, L. Huang, Q. Zhang, Improvement of visible light photocatalytic activity over flower-like BiOCl/BiOBr microspheres synthesized by reactable ionic liquids, Colloid Surf. A 420 (2013) 89–95.
[56] J. Xia, S. Yin, H. Li, H. Xu, L. Xu, Y. Xu, Improved visible light photocatalytic activity of sphere-like BiOBr hollow and porous structures synthesized via a reactable ionic liquid, Dalton Trans. 40 (2011) 5249–5258.
[57] M. Li, H.W. Huang, S.X. Yu, N. Tian, F. Dong, X. Du, Y.H. Zhang, Simultaneously promoting charge separation and photoabsorption of BiOX (X = Cl, Br) for efficient visible-light photocatalysis and photosensitization by compositing low-cost biochar, Appl. Surf. Sci. 386 (2016) 285–295.
[58] J.F. Zhang, W.L. Yu, J.J. Liu, B.S. Liu, Illustration of high-active Ag_2CrO_4 photocatalyst from the first-principle calculation of electronic structures and carrier effective mass, Appl. Surf. Sci. 358 (2015) 457–462.
[59] J.J. Liu, S.F. Chen, Q.Z. Liu, Y.F. Zhu, J.F. Zhang, Correlation of crystal structures and electronic structures with visible light photocatalytic properties of $NaBiO_3$, Chem. Phys. Lett. 572 (2013) 101–105.
[60] X.-j. Wang, Y. Zhao, F.-t. Li, L.-j. Dou, Y.-p. Li, J. Zhao, Y.-j. Hao, A chelation strategy for in-situ constructing surface oxygen vacancy on {001} facets exposed BiOBr nanosheets, Sci. Rep. 6 (2016) 24918.
[61] K. Dai, G. Dawson, S. Yang, Z. Chen, L. Lu, Large scale preparing carbon nanotube/zinc oxide hybrid and its application for highly reusable photocatalyst, Chem. Eng. J. 191 (2012) 571–578.
[62] J. Jin, J.G. Yu, D.P. Guo, C. Cui, W. Ho, A hierarchical Z-scheme CdS-WO_3 photocatalyst with enhanced CO_2 reduction activity, Small 11 (2015) 5262–5271.
[63] J. Jiang, X. Zhang, P. Sun, L. Zhang, ZnO/BiOI heterostructures: photoinduced charge-transfer property and enhanced visible-light photocatalytic activity, J. Phys. Chem. C 115 (2011) 20555–20564.